Advanced Materials Interfaces

ADVANCED MATERIALS INTERFACES Open Access

www.advmatinterfaces.de

RESEARCH ARTICLE OPEN ACCESS

Maskless Fabrication of PLA-Based Neural Arrays for CNS Recording and Stimulation

Anna De Salvo[1] | Federica Velluto[1,2] | Ilenia Sergi[1,2] | Michele Di Lauro[1] | Verónica Barranco-Maresca[3,4] | Elena Alonso-Calviño[4,5] | Yasmina Hernández-Martín[4,6] | Juan Aguilar[5,4,7] | Juliana M. Rosa[3,4,7] | María C. Serrano[8] | Carolina Giulia Ferroni[2] | Federico Rondelli[1] | Elisa López-Dolado[4,6,7] | Luciano Fadiga[1,2] | Fabio Biscarini[1,9]

[1]Center for Translational Neurophysiology of Speech and Communication, Fondazione Istituto Italiano di Tecnologia (IIT-CTNSC), Ferrara, Italy | [2]Sezione di Fisiologia, Dipartimento di Neuroscienze e Riabilitazione, Università di Ferrara, Ferrara, Italy | [3]Neuronal Circuits and Behaviour Group, Hospital Nacional de Parapléjicos, Toledo, Spain | [4]Instituto de Investigación Sanitaria de Castilla-La Mancha (IDISCAM), Toledo, Spain | [5]Experimental Neurophysiology Group, Hospital Nacional de Parapléjicos, Toledo, Spain | [6]Laboratory of Interfaces for Neural Repair, Hospital Nacional de Parapléjicos, Toledo, Spain | [7]Design and development of biomaterials for neural regeneration, HNP, Associated Unit to CSIC through ICMM, Toledo, Spain | [8]Instituto de Ciencia de Materiales de Madrid (ICMM), CSIC, Madrid, Spain | [9]Life Sciences Dept., Università di Modena e Reggio Emilia, Modena, Italy

Correspondence: Michele Di Lauro (michele.dilauro@iit.it)

Received: 29 April 2026 | **Revised:** 24 June 2026 | **Accepted:** 8 July 2026

Keywords: bidirectional | brain | multi-electrode arrays | neurotechnologies | spinal cord | transient electronics

ABSTRACT

Micro-electrode arrays based on poly-lactic acid substrates featuring gold electrodes coated with poly(3,4-ethylenedioxythiophene)/poly(styrenesulfonate) are fabricated via maskless wet-techniques and subtractive laser patterning. Devices exhibit stable electrical performance at the bench-side over weeks and enable high-quality neural interfacing in acute in vivo experiments. Two device layouts are presented: one for micro-epicorticography and one for spinal cord stimulation. Cortical arrays are benchmarked against somatosensory evoked potentials in bilateral micro-electrocorticography, showing robust contralateral activation and negative ipsilateral control. Spinal arrays activate sensory and motor pathways according to spatial features of the injected electric field, at fixed stimulation frequency and intensity, thus demonstrating localized stimulation. Long-term (4-months) implantation of spinal arrays results in almost complete substrate degradation and good device biocompatibility. These results demonstrate a versatile and sustainable fabrication workflow for prototyping of biodegradable substrate-based neural interfaces, which opens new opportunities for transient neuroelectronics tailored to the application and the patient.

1 | Introduction

Neural interfaces addressing both the central and peripheral nervous systems were developed to probe and modulate neural activity. Moving from rigid to flexible devices resulted in better coupling and a conformal interface with soft neural tissue [1, 2], thus enabling dynamic mapping of electrophysiological signals, either spontaneous or elicited, across different regions of the nervous system [3].

One of the main challenges in neural interfaces is to extend the timescale of implant toleration by the body. This aim is pursued by making the implanted devices as mechanically compliant as possible to the target area, with the aim of minimizing the risks of inflammation and rejection due to foreign body reaction [4, 5]. While some implants are intended to be life-long, some others exert their action for a limited amount of time. As such, they should either be removed with a second surgical intervention or should be left in the body. Both cases result

in additional risks for patients, including iatrogenic infections during the second surgical procedure or glial scarring around the implant. In this scenario, transient neurotechnologies may represent a viable alternative, as they can exhibit a tailored operational lifetime before being resorbed after performing their function [6–8].

The transient approach to clinical issues is producing an impressive technological throughput in terms of biodegradable electronic components, expanding the range of possible strategies to design fully biodegradable biomedical circuitry, electrical stimulators, sensors, and transient complementary metal-oxide-semiconductor (CMOS) devices [9–11]. Biodegradable materials are widely used in regenerative medicine, especially in scaffolds for the treatment of central and peripheral neural lesions, to restore and promote cellular regrowth and reconnection [12, 13].

When it comes to interfacing the central nervous system with transient electronics, brain implants and spinal implants are nowadays at two different developmental stages. On the one hand, in the brain, synthetic biodegradable polymers such as poly-lactic acid (PLA) [14–16] and its copolymers, as well as conductive hydrogels [17], were used for manufacturing recording devices lasting up to almost one month [16, 18]. Yet, demonstration of biodegradable implants to interface the spinal cord is still lacking, despite the tremendous advancements made in the field of spinal interfaces, with implants based on non-biodegradable polyimide or PDMS [19–24].

Biodegradable PLA exhibits intermediate intrinsic mechanical properties compared to conventional substrate materials—its Young's modulus (2–4 GPa) lies well below that of polyimide (~9 GPa) but far above soft elastomers such as PDMS (<1 MPa). However, in thin-film neural interfaces the effective mechanical behaviour is largely governed by geometry and thickness rather than by the bulk material properties [25–29].

In this work, we present multi-electrode cortical (MEcA) and spinal (MEsA) arrays fabricated on the clinically established biodegradable PLA [30–32] as substrate and insulating layer. Unlike conventional microfabrication workflows — typically relying on photolithographic processes involving masks, multiple deposition steps, and chemical etching — our approach is entirely maskless, based on solution processing and laser ablation. The entire process relies on three steps, namely solution casting, spin-coating, and laser patterning, which can be extended to larger substrates or higher-density electrode arrays, coupling high throughput with prototyping versatility. Decoupling device manufacturing from photolithographic mask approach greatly increases the accessibility of biodegradable neurotechnology and opens the possibility for distributed and tailored manufacturing of personalized devices. This work contributes an integrated fabrication strategy that combines maskless processing on biodegradable PLA with the first biodegradable epidural stimulator and enables the realization of devices for both cortical recording and spinal stimulation, addressing a current gap in transient neural interfaces. MEcAs and MEsAs feature electrodeposited poly(3,4-ethylenedioxythiophene)/poly(styrenesulfonate) (PEDOT/PSS) as a functional coating for the electrode sites to yield low-impedance interfaces suitable for acute neurophysiological applications with enhanced recording and low voltage stimulation [33].

The operational lifetime of MEcAs and MEsAs is assessed via bench-side accelerated aging tests aimed to simulate the degradation processes occurring in vivo upon prolonged implantation [16, 18, 34].

Electrophysiological performance of the proposed architectures is evaluated in acute in vivo experiments, by interfacing them with state-of-the-art neural acquisition and stimulation systems, for MEcAs and MEsAs, respectively. Additionally, MEsAs in vivo biodegradation and biocompatibility are characterized in a chronic scenario, up to four months, by immunofluorescence.

2 | Results and Discussion

2.1 | Design and Additive Fabrication of Transient Electronic Neural Arrays

MEcAs and MEsAs are fabricated using the maskless fabrication approach illustrated in Figure 1. In line with the state of the art in clinical neurotechnology [19, 29, 35–39], circular electrodes are used for MEcAs while elongated ones are used for MEsAs.

MEcAs are designed to be interfaced with small areas of the rat brain cortex. More specifically, they are addressed to the rat barrel field, which typically spans an area between 4 and 6 mm^2 [40]. Accordingly, the MEcAs working area (WA)— defined as the areal portion including exposed electrode sites –is a square of 1.5 mm x 1.5 mm (WA = 2.25 mm^2), featuring 9 circular electrode sites (Ø = 300 µm) in a 3×3 grid.

MEsAs designed to stimulate the spinal cord on both sides of a hypothetical one-vertebra-long lesion need an active area roughly three vertebrae long and as wide as the spinal cord, about 2–4 mm in rats [41, 42]. Hence, the MEsA's working area measures 1 mm in width and 4.5 mm in length, hosting 11 elliptical electrodes (major axis: 500 µm; minor axis: 300 µm).

Both layouts have a total length of 3.5 cm and a shank width of 2 mm. In MEcAs, inter-lead clearance is 100 µm, with individual lead widths of 60 µm along the routing area. For the MEcA configuration, the inter-lead clearance is set to 80 µm, with lead widths of 60 µm along the routing area. Both layouts are designed to be hosted by a zero-insertion-force (ZIF) connector, mounted on a custom-designed PCB.

The PLA-based microelectrode arrays are fabricated through a multilayer process combining sacrificial poly-acrylic acid (PAA) layers, PLA casting, metal patterning, and thermal sealing. Full fabrication details are provided in the Experimental Section. Briefly, two water-soluble PAA sacrificial layers are first spin-coated onto glass Petri dishes and thermally cured. A PLA solution is then cast onto each PAA layer and left to evaporate at room temperature before undergoing a second curing step (Figure 1a). From the first PAA/PLA stack, a free-standing PLA film is obtained by dissolving the PAA in water for 24 h. This PLA layer serves as the insulator and is patterned by laser ablation to

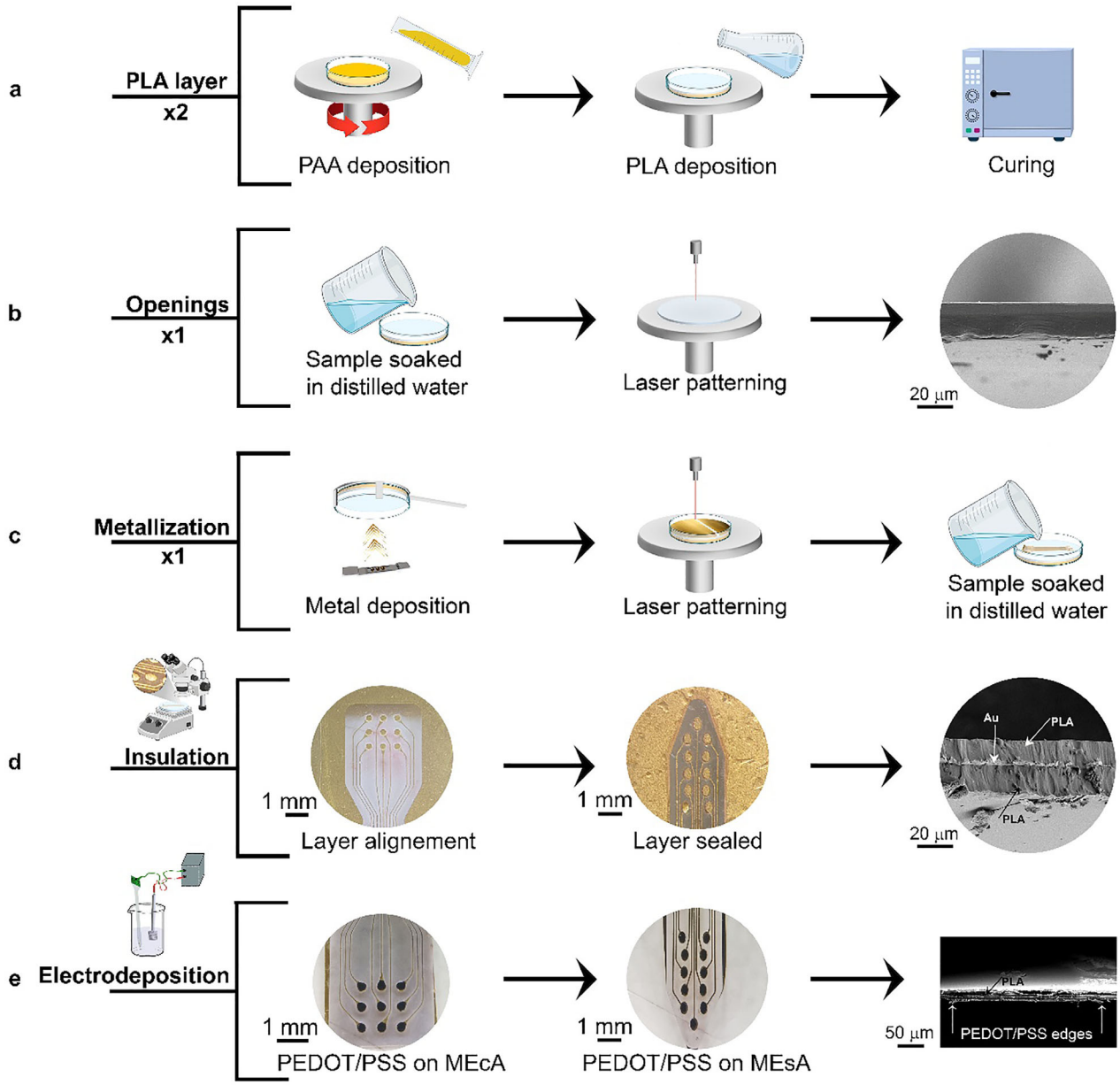

FIGURE 1 | (a) PAA/PLA stacked structure. (b) PLA free-standing film for openings on the insulation layer. SEM image of a PLA layer section. (c) PAA/PLA metallization. (d) Alignment and thermal sealing of electrodes pattern and PLA insulation layer. SEM image of the PLA/Ti/Au/PLA stacked structure. (e) Electrodeposition of PEDOT/PSS on MEcA and MEsA. SEM image of the electrode section highlighting the PEDOT/PSS covered electrode edges.

define electrode and pad openings. The resulting film exhibits a thickness of 18 ± 1 µm, as confirmed by SEM cross-section imaging (Figure 1b). The second PAA/PLA stack is metallized with a Ti/Au bilayer (5 nm/70 nm) and patterned by laser ablation to define the electrode array. After lift-off in water, a free-standing PLA/Ti/Au microelectrode layer is obtained (Figure 1c). The metallized layer and the insulating PLA film are aligned under optical microscopy, exposing only electrode sites and connector pads, and subsequently thermally sealed (Figure 1d). The final device thickness is 30 ± 2 µm (N = 3), as shown in the SEM cross-section image. A polyimide spacer is attached to the backside of the connector region to ensure reliable electrical interfacing. Finally, a PEDOT/PSS coating is electrodeposited onto the gold electrodes. Through SEM imaging, the PEDOT/PSS thickness is estimated at 555 ± 165 nm (Figure 1e and Figure S1). AFM analysis further confirms the expected globular morphology of evaporated Au (RMS roughness 2.7 nm) and the characteristic granular microstructure of freshly electrodeposited PEDOT/PSS, which exhibits an RMS roughness of 8.2 nm and a short correlation length (4.5 nm), consistent with a compact and homogeneous film (Figure S2).

2.2 | Device Electrochemical Characterization

Electrochemical impedance spectroscopy (EIS) and chronopotentiometry techniques are used to characterize the designed probes (Figure 2). Figure 2a, b shows the Bode and phase plots of both

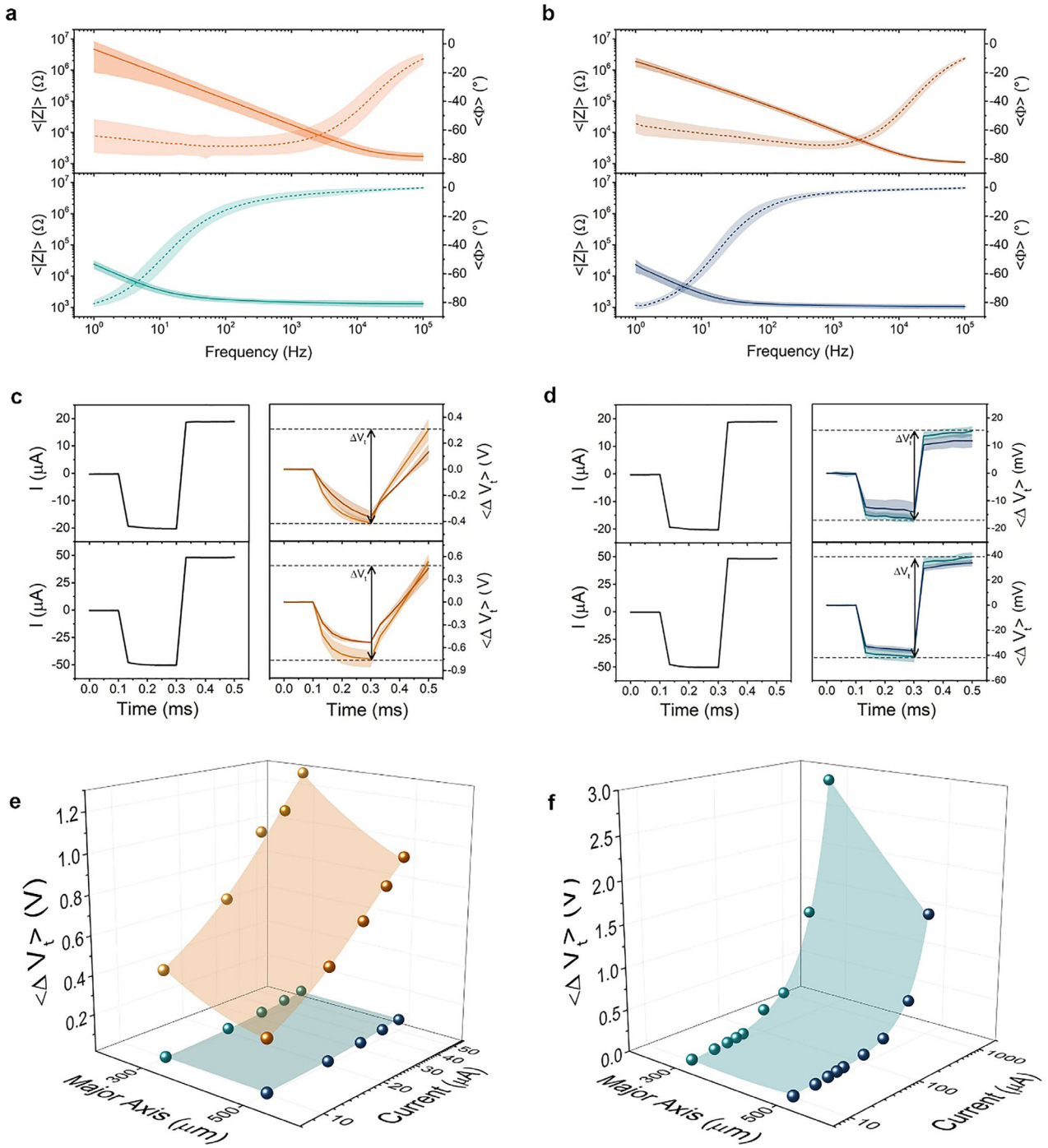

FIGURE 2 | (a) Impedance modulus of MEcA's bare gold electrodes (Top) and MEcA's PEDOT/PSS covered electrodes (Bottom). (b) Impedance modulus of MEsA's bare gold electrodes (Top) and MEsA's PEDOT/PSS covered electrodes (Bottom). The shaded area in (a) represents the standard deviation over N = 63 samples and in (b) represents the standard deviation over N = 77 samples. (c) On the left, the biphasic current pulse delivered for the characterization with a half-amplitude equal to 20 μA (Top) and 50 μA (Bottom). On the right, the average voltage transient elicited at the electrode/electrolyte interface of MEcAs (orange line) and MEsAs (dark orange line) with bare gold electrodes. (d) On the left, the biphasic current pulse delivered for the characterization with a half-amplitude equal to 20 μA (Top) and 50 μA (Bottom). On the right, PEDOT/PSS covered electrodes averaged voltage transient. Green line is from MEcAs electrodes, dark blue line is from MEsAs electrodes. The shaded areas both in (c) and in (d) represent the standard deviations over N = 6 samples. (e) 3D plot showing the dependence of the voltage transient ΔV_t vs the major axis (300 μm for MEcAs and 500 μm for MEsAs electrodes) and the delivered current (half-amplitude between 10 and 1000 μA) and the delivered current. The blue surface represents the distribution for PEDOT/PSS electrodes, while the light orange surface indicates the distribution for gold electrodes. Both surfaces are provided as a guide to the eye. (f) 3D plot showing the dependence of the transient voltage ΔV_t on both the major axis (300 μm for MEcAs and 500 μm for MEsAs electrodes) and the delivered current (half-amplitude between 10 and 1000 μA) for PEDOT/PSS coated electrodes. The blue surface represents the distribution for PEDOT/PSS electrodes and acts as a guide to the eye.

uncoated and coated electrodes. At 1 kHz, the MEcAs gold electrodes exhibit an impedance modulus of 17 (± 7) kΩ, meanwhile MEsAs bare electrodes feature an averaged impedance modulus of 12 (± 2) kΩ. Coated electrodes are characterized by an overall decrease of the impedance modulus across the entire frequency range, with a 90% reduction at 1 kHz compared to bare electrodes. The geometrical difference between MEcAs and MEsAs PEDOT/PSS covered electrodes further result in a decrease in impedance modulus from 1.3 (± 0.2) to 1.0 (± 0.1) kΩ at 1 kHz, respectively. Overall reproducibility of electrodes performance is evaluated by considering the impedance at 1 kHz across 10 devices featuring PEDOT/PSS covered electrodes for each design and from different fabrication round (Figure S4).

To evaluate the polarization voltage required to deliver controlled current pulses from MEcAs to MEsAs, chronopotentiometry experiments are performed. For stimulation devices, it is generally desirable to maintain the electrode interfacial potential within a voltage range that prevents irreversible redox reactions in aqueous environments. Such reactions may degrade the electrodes, damage tissue, and decrease the stimulation efficacy by increasing the charge-injection threshold. Based on cyclic voltammetry data (Figure S3), the electrochemically safe window for PEDOT/PSS-coated electrodes can be identified between −0.5 and 0.7 V, meanwhile for bare gold electrodes between −0.4 and 0.6 V. In this operational window, coated electrodes exhibit charge-storage capacity values of 2.2 ± 0.2 mC cm^{-2} for MEcA and 3.8 ± 0.4 mC cm^{-2} for MEsA (mean ± SD, n = 3). Figure 2c, d shows the voltage transients (ΔV_t) elicited at the electrode/electrolyte interface for bare and PEDOT/PSS-coated electrodes from MEcAs to MEsAs under peak-to-peak current pulses of 40 and 100 μA. The complete set of voltage transient measurements, for both bare and coated electrodes, are reported in Figure S5. The voltage transients are evaluated by selecting the peak-to-peak amplitude of the elicited voltages between 200 and 400 μs (Figure 2c, d). For bare gold electrodes (Figure 2c), it is evident that, for a fixed current, the polarization voltage at the electrode/electrolyte interface decreases as the electrode geometrical area increases.

The same trend is observed in PEDOT/PSS covered electrodes (Figure 2d), albeit with lower amplitudes and narrower distribution with respect to bare electrodes. This large difference concerning voltage transients is dramatic in the three-dimensional plot in Figure 2e, which shows ΔV_t as a function of both the delivered current amplitude and the electrodes' major axis for gold bare and coated electrodes. PEDOT/PSS-coated electrodes – regardless of their major axis – exhibit ΔV_t values between 10 and 70 mV, based on the grand average across all tested current amplitudes and electrode dimensions (N = 60). This yields a nearly flat surface in the 3D graph representation (Figure 2e). In contrast, ΔV_t for bare gold electrodes increases with current amplitude and decreases with the electrode major axis.

PEDOT-coated electrodes with small-diameter (100–200 μm) and short pulse widths (200 μs) are known to yield high CIC values (2–6 mC cm^{-2}) [43, 44]. Conversely, larger electrodes operated with longer pulse widths report usually result in lower CIC values per phase (0.2–0.60 mC cm^{-2}, considering only the anodic or the cathodic phase of the pulse) [45]. Within this framework, our electrodes exhibit CIC values of 0.14 and 0.16 mC/cm^2 and current limits of 0.5–1 mA for a pulse width of 200 μs, which are consistent with expectations for large-area PEDOT/PSS electrodes operated at short pulse widths.

It is worth noting that, to achieve polarization voltages comparable to those obtained with bare gold electrodes at currents between 20 and 100 μA, PEDOT/PSS-coated electrodes require much higher currents, between 500 and 1000 μA (Figure 2f).

PEDOT/PSS-coated electrodes exhibit voltage transients that are, on average, more than 15-fold lower than those of bare gold electrodes, regardless of electrode geometry. On the basis of these comparisons, showing the crucial benefits of PEDOT/PSS coating, [46], it has been decided to assess the aging, the electrophysiological performances and the foreign body reaction only for MEcAs and MEsAs featuring electrodes with organic coating.

2.3 | Impact of Aging on Arrays and Electrochemical Impedance Spectroscopy

The degradation of the PLA-based neural interfaces is assessed through an in-vitro ageing test performed in 1 M PBS at pH 7.4 and 40°C(Figure 3).

The bath temperature is monitored using a temperature sensor connected to a wireless platform that records temperature values every 30 s (Figure S6). Time-lapse imaging and electrochemical impedance spectroscopy are performed every seven days to monitor the condition of the arrays. The experimental setups are shown in Figure S6. Figure 3a, b illustrates the degradation timeline for the MEcAs and MEsAs. Overall, the probes maintained their structural integrity throughout the investigated period, without any notable changes in their appearance.

The impact of degradation on MEcAs and MEsAs electrodes, assessed through EIS measurements is reported in Figure 3c, d as average Bode plots for day 1 and day 28. Full datasets are provided in Figure S7. The test included 26 electrodes for MEcAs (three devices) and 33 electrodes for MEsAs (three devices). Bode plots show only minimal variations in the PEDOT/PSS electrodes (Figure 3c, d). The slight modulation of both impedance magnitude and phase suggests hydration, swelling and stabilization of the PEDOT/PSS film in the electrolytic environment, with no evidence of gold exposure or deterioration of the insulating layer. AFM analysis after 28 days of aging (Figure S2) further supports these observations, showing a marked increase in roughness (17.6 nm) and in correlation length (7.6 nm), consistent with swelling-induced rearrangement of the polymer network. This morphological evolution aligns with the modest impedance reduction observed during ageing (∼5% for MEsA and ∼15% for MEcA at 1 kHz).

As shown in Figures S8 and S9, despite the bending of the arrays during the ageing test, electrochemical measurements were still performed, providing insight into their mechanical stability—at least under bench-side conditions. The possibility to acquire EIS measurements after 28 days is consistent with the time-lapse images and with previous work that used PLA as insulation layer [47].

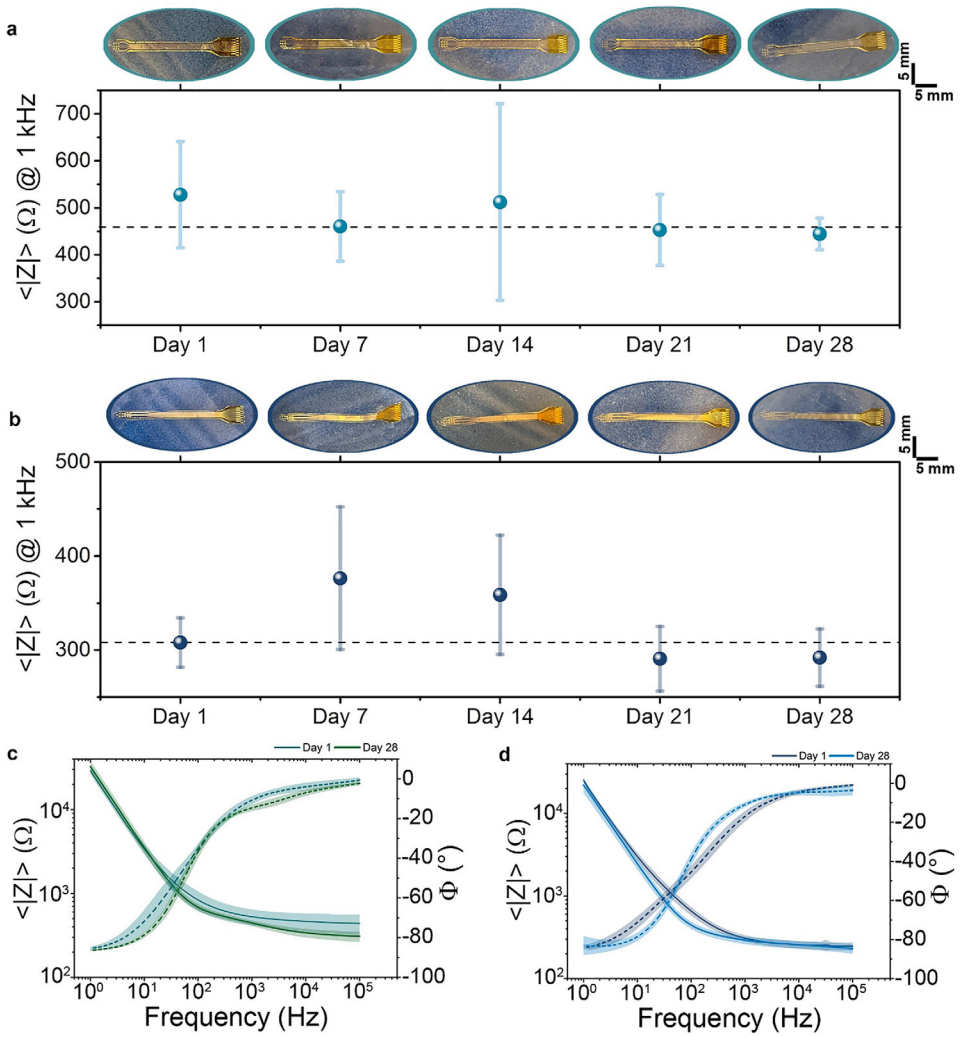

FIGURE 3 | (a) MEcA optical image during ageing test together with the mean impedance at 1 kHz acquired at 7-day intervals. (b) MEsA optical image during the ageing test together with the mean impedance at 1 kHz acquired at 7-day intervals. Dashed lines in (a) and (b) represent the median. Error bars represent the standard deviation. (c) Averaged EIS and phase for MEcA electrodes. Aqua green lines represent the EIS (continuous line) and phase (dashed line) measurements acquired on the 1st day. Aqua green shades represent the standard deviation across 26 samples. Light green lines represent the EIS (continuous line) and phase (dashed line) measurements acquired on the 28th day. Green shade represents the standard deviation across 18 samples. (d) Averaged EIS and phase for MEsA electrodes. Dark blue lines represent the EIS (continuous line) and phase (dashed line) measurements acquired on the 1st day. Blue shades represent the standard deviation across 33 samples. Light blue lines represent the EIS (continuous line) and phase (dashed line) measurements acquired on the 28th day. Light blue shades represent the standard deviation across 29 samples.

During the 28-day EIS monitoring, impedance spectra are successfully collected from all 26 MEcAs electrodes and all 33 MEsAs electrodes during the first 14 days. After the third week, the number of readable electrodes began to decrease. This reduction is attributed to deterioration of the contact pads, which impaired reliable electrical connection between the devices and the measurement setup (Figures S8b and S9b).

2.4 | Bilateral Micro-Electrocorticography with Biodegradable Arrays

Bilateral micro-electrocorticography recordings are performed in N = 2 rats in an acute experiment (Figure 4). In each animal, two MEcA arrays are implanted epidurally over the barrel cortex (Figure 4a, h) following standard neurosurgical exposure, as detailed in the Experimental Section.

Epicortical signals are recorded simultaneously from the contralateral and ipsilateral hemispheres during right-side single-pulse whisker stimulation to assess recording performance through somatosensory evoked potentials (SEPs) [48, 49], providing both the evoked response and an internal ipsilateral control. Arrays are positioned as symmetrically as possible over corresponding whisker-related cortical areas, and data are acquired using an Intan RHD system. The TTL output of the stimulator is recorded to enable precise temporal alignment and averaging of evoked responses, allowing direct contralateral–ipsilateral comparisons. Each recording session includes 60 trials per position. Further details are provided in the Experimental

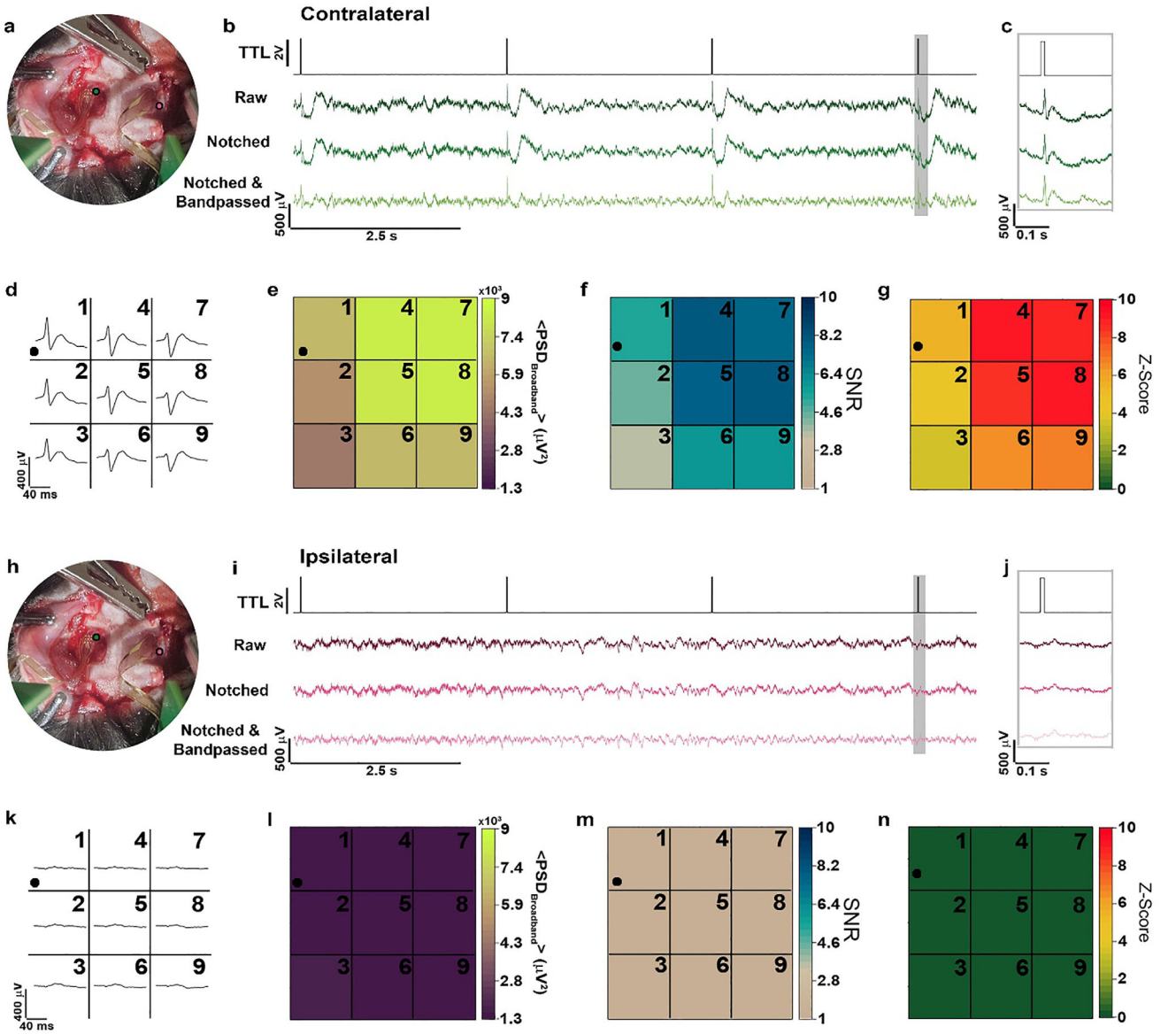

FIGURE 4 | (a) and (h) Images of the implantation site (somatosensory cortex-barrel cortex) for the bilateral recording session. Black/colored dots indicate the position of electrode 1 on the contralateral (green center) and ipsilateral (pink center) cortex. (b) Contralateral 10-s recording trace representing the TTL traces, raw trace (dark green), notched trace (green), and band-passed trace (light green). The grey area highlights the zoomed portion of the trace time-locked to the TTL pulse, shown in (c). (d) Averaged SEPs responses recorded by the nine electrodes on the barrel cortex area. (e) SEPs signal power across electrodes on the grid. (f) Signal-to-noise ratio of somatosensory evoked responses. (g) Z-score of somatosensory evoked responses. (i) Ipsilateral 10-s recording trace representing the TTL traces, raw trace (purple), notched trace (pink), and band-passed trace (light pink). The grey area highlights the zoomed portion of the trace time-locked to the TTL pulse, shown in (j). (k) Averaged responses recorded by the nine electrodes on the ipsilateral barrel cortex area. (l) Spontaneous activity signal power across electrodes on the grid. (m) Signal-to-noise ratio of spontaneous activity. (n) Z-score of spontaneous activity. Where present, the black dot indicates the position of electrode 1 on the cortex.

section. In Figure 4b, i, 10 s of a representative recording session are shown (Rat = 1, position 1). TTL pulses, raw data, notched, and band-passed signals are reported to compare the effects of filtering on the recordings. Details on the data analysis are reported in the Experimental section. The evoked potential in the contralateral hemisphere is clearly visible, from the raw traces through the band-passed signals. When zooming in on the traces at the time of a TTL pulse (Figure 4c,j), the SEP is evident on the contralateral side, whereas neither events nor TTL-related artifacts are detected on the ipsilateral side.

Figure 4d,k presents the averaged SEPs and ipsilateral activity across 60 trials, displayed in a 3×3 grid reflecting the spatial arrangement of the electrodes within the cortical area. This representation highlights the evolution of the evoked responses recorded at different electrode positions over the same cortical region, albeit in both hemispheres. To complement these traces, power maps are computed (Figure 4e,l) by integrating the power spectral density (PSD) between 5 and 300 Hz. These maps support the spatial distribution of signal power for the SEPs, with localized increases corresponding to contralateral cortical activation, whereas the ipsilateral activity shows a

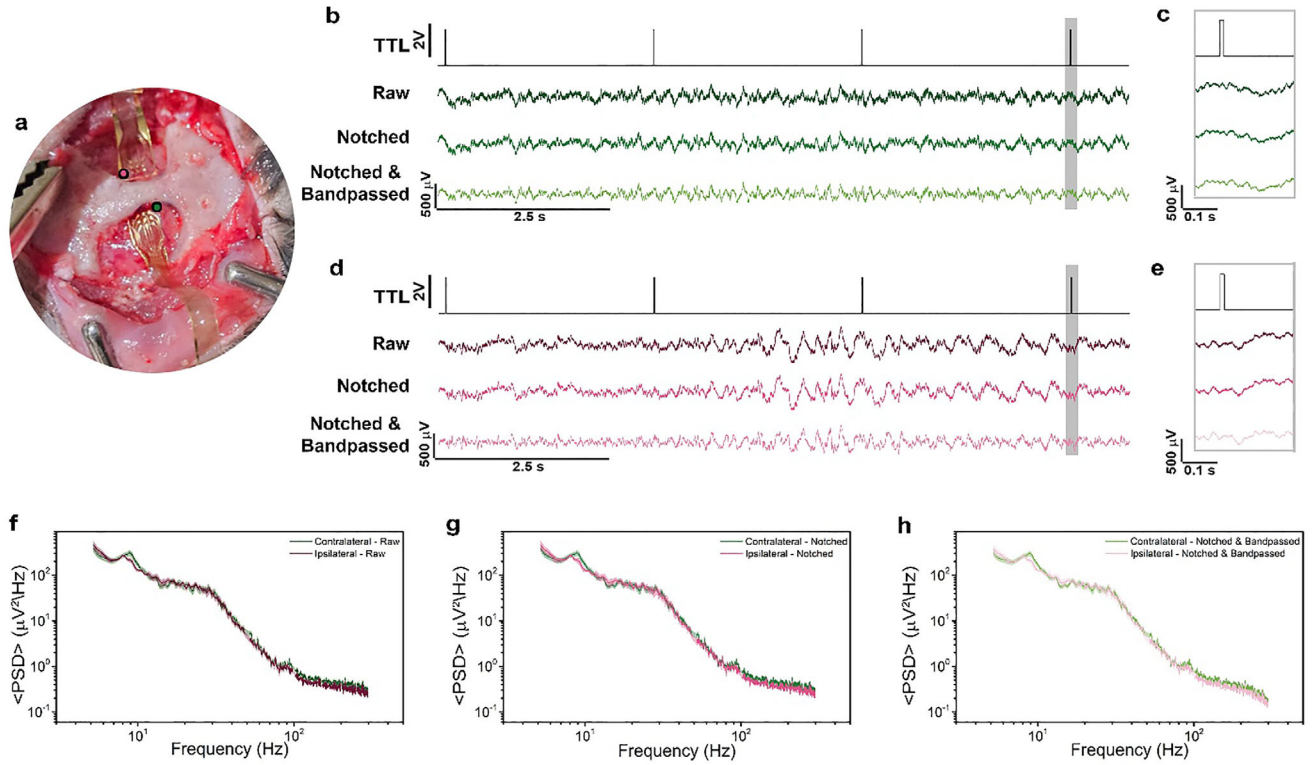

FIGURE 5 | (a) Image of the implantation site (Parietal Cortex) for the bilateral recording session. Black/colored dots indicate the position of electrode 1 on the contralateral (green center) and ipsilateral (pink center) cortex. (b) Contralateral 10-s recording trace in Parietal Cortex representing TTL trace, raw trace (dark green), notched trace (green), and band-passed trace (light green). The grey area highlights the zoomed portion of the trace time locked to the TTL pulse, shown in (c). (d) Ipsilateral 10-s recording trace in Parietal Cortex representing TTL trace, raw trace (purple), notched trace (pink) and band-passed trace (light pink). The grey area highlights the zoomed portion of the trace time locked to the TTL pulse, shown in (e). (f) Contralateral (dark green) vs. ipsilateral (purple) averaged Power Spectral Density of the 2-min raw signal recorded by the nine electrodes. (g) Contralateral (green) vs. Ipsilateral (pink) averaged Power Spectral Density of the 2-min notched signal recorded by the nine electrodes. (h) Contralateral (light green) vs. Ipsilateral (light pink) averaged Power Spectral Density of the 2-min band-passed signal recorded by the nine electrodes.

nearly constant power distribution across electrodes. Full traces from the nine recording channels, together with averaged signals superimposed on the 60 individual trials, are shown in Figure S10.

To quantitatively assess the quality and reliability of the recorded neural signals, we evaluate the Signal-to-noise ratio (SNR) (Figure 4m, f) and Z-score (Figure 4 g, n) at each electrode. These metrics are widely used in acute epidural micro-ECoG recordings because they normalize the evoked response relative to baseline variability and are largely independent of electrode-to-source distance, which can vary slightly across acute sessions. SNR is computed as the ratio between the power of the evoked response in an 80 ms window and spontaneous activity in an equivalent window 1 s before stimulation. Z-scores are computed using the same segmentation of the signal. A consistent colour map is applied to both datasets to enable direct comparison. Across the grid in the contralateral condition, both SNR and Z-score range from 3 to 10. Ipsilateral traces show unitary SNR and Z-score, confirming the spatial specificity of the evoked responses. Electrode-wise SNR and Z-score values (mean ± SEM across 60 trials) are reported in Tables S1–S4.

As an additional control, bilateral micro-electrocorticography recording is performed in the parietal cortex (Figure 5a) during whisker stimulation to exclude potential effects of cortical synchronization (Rat 1 – position 2).

Ten seconds of the recording session are shown in Figure 5b, d under the same three conditions as in Figure 4b, i. In the magnified traces corresponding to a single TTL pulse (Figure 5c, e), neither recording exhibits events or artifacts related to TTL. Additionally, the 2 min recording traces are compared in terms of power spectral density within the 5–300 Hz range. Overall, the spectral behaviour is comparable. Additional recording sessions supporting these findings are reported in Figures S11–S14.

2.5 | Spinal Cord Stimulation with Biodegradable Arrays

To assess stimulation performance, MEsAs are positioned epidurally over the exposed rat spinal cord in N = 4 rats (one MEsA per animal), and input–output curves experiments are carried out in both crossed and linear bipolar configurations (Figure 6). Details regarding the surgical procedure, signal acquisition, and data processing are provided in the Experimental section.

To evaluate the recruitment and selective activation of distinct motor and sensory pathways upon controlled-current stimulation

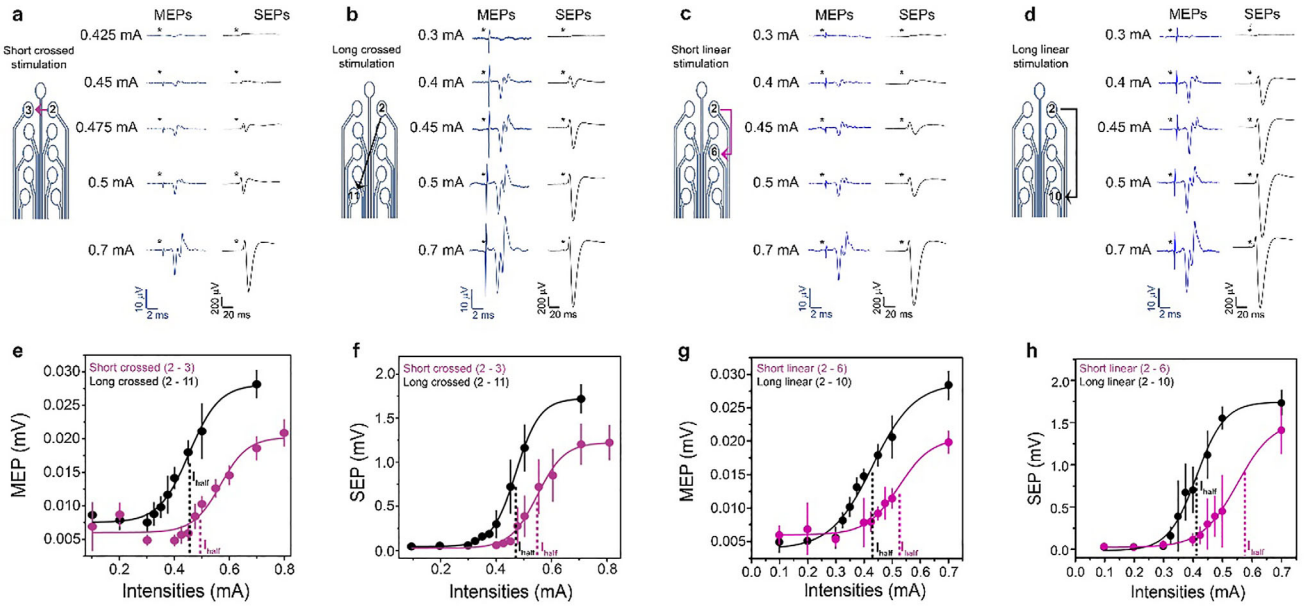

FIGURE 6 | (a) MEPs (blue) and SEPs (black) traces showing the increasing amplitude of the responses as a function of increasing intensities in the short-distance crossed configuration. (b) MEPs (blue) and SEPs (black) traces showing the increasing amplitude of the responses as a function of increasing intensities in the long-distance crossed configuration. (c) MEPs (blue) and SEPs (black) traces showing the increasing amplitude of the responses as a function of increasing intensities in the short-distance linear configuration. (d) MEPs (blue) and SEPs (black) traces showing the increasing amplitude of the responses as a function of increasing intensities in the long-distance linear configuration. The asterisk represents the time point of stimulation and the respective artifact. All tracings correspond to a single rat (Rat 1). (e) and (f) Input–output curves for MEPs and SEPs showing the population response for short-distance (magenta) and long-distance (black) crossed configurations. (g) and (h) Input–output curves for MEPs and SEPs showing the population response for short-distance (magenta) and long-distance (black) linear configurations. Dots represent the average value from 50 to 100 stimuli reported with the standard error value and dashed lines represent the I_{half} value.

of the lumbar spinal region (L1-L3), the array is positioned with the spinal midline aligned between the two electrode rows (Figure S15). This configuration, combined with variations in stimulation geometry (crossed vs linear; short vs long inter-electrode distance), enables selective activation of distinct motor and sensory pathways. Simultaneous electroencephalography (EEG) and electromyography (EMG) recordings are acquired to measure SEPs, reflecting activation of the ascending gracile dorsal column pathway, and the motor evoked potentials (MEPs) in response to lumbar motor circuit recruitment.

Figure 6a, b shows SEPs and MEPs recorded in one representative session (Rat 1) during crossed stimulation. In this configuration, both SEPs and MEPs amplitudes scale coherently with the stimulation intensity, consistent with progressive recruitment of local sensory and motor circuits. Notably, SEPs are elicited at substantially lower intensities than MEPs, this is consistent with the anatomical organization of sensory and motor pathways in the spinal cord.

Long-distance crossed configurations (e.g., electrodes 2–11) evoke larger SEPs and MEPs than short-distance configurations (e.g., electrodes 2–3). The stimulation intensity required to reach 50% of the maximal response (I_{half}) is correspondingly lower for long-distance configurations (Figure 6e, f), although inter-animal variability is observed (Figures S16–S18).

Linear stimulation produces a similar pattern of activation (Figure 6c, d). Increasing the inter-electrode distance results in larger evoked responses in both EEG and EMG, with long-distance configurations generating higher-amplitude SEPs and MEPs (Figure 6 g, h).

For motor responses, the long-distance electrode configurations are more effective at recruiting spinal motor neurons, producing larger motor evoked potentials (MEPs) and requiring lower I_{half} compared to short-distance configurations. Moreover, the lowest stimulation threshold is observed in the linear long-distance electrode configuration. This likely reflects activation of motor neurons across different spinal segments, which is important since limb muscles receive input from more than one segment.

Short-distance configurations, while less effective in terms of amplitude, provide more spatially focused activation, which may be advantageous when selective recruitment of specific spinal segments is desired.

For sensory responses, measured as SEPs, long-distance configurations similarly produce stronger responses, indicating more effective activation of the gracile fasciculus. Inter-animal variability is observed, likely reflecting small anatomical differences and fine variations in electrode placement over the dorsal surface of the spinal cord (Figures S16–S18). Such variability is physiologically meaningful: broader recruitment in long configurations may engage inhibitory mechanisms in subcortical structures such as the gracile nucleus or ventral posterolateral thalamus (VPL), leading to lateral inhibition and to a reduction in cortical SEP amplitudes. In contrast, short configurations may activate

a more localized set of afferents, avoiding lateral inhibition and potentially promoting feedforward disinhibition, as previously reported [50–52]. This interpretation is supported by individual animal results.

2.6 | In Vivo Biodegradability and Biocompatibility

Finally, we investigate the in vivo biodegradability and biocompatibility of the MEsAs when chronically implanted epidurally over the cervical spinal cord of N = 3 rats. The device is positioned after removing the C5–C7 laminae, allowing stable contact between the array and the meninges (Figure 7a). The sharp end of the arrays is gently slid underneath the C4 lamina to enhance mechanical stability, and a Neuro-patch (4×6 mm^2) is placed on top of the device. The removed vertebral laminae are then repositioned to reinforce the cervical column. Details of the chronic epidural array implantation surgery are reported in the Experimental Section.

The peripheral section of the arrays, housing the contact pads, remains accessible for approximately one month before being disrupted by mechanical stresses from muscle and skin closure.

Implanted rats are maintained for four months after implantation without evident signs of behavioral alterations, weight loss or major toxicity symptoms. When rats are sacrificed, the arrays are no longer identifiable except for the gold contacts adherent to the meninges (Figure 7b), indicating complete biodegradation of the PLA substrate. Macroscopic observation of the cervical spine did not reveal noticeable differences with respect to the controls (Figure 7c).

Immunofluorescence analysis of the cervical spinal tissue further confirms the macroscopic observation (Figure 7d). The presence of the electrode arrays on top of the spinal cervical region increased cell density (measured as the positive area of cell nuclei stained with Hoechst; *Student's t-test*, $p < 0.001$). Indeed, the number of cells augmented by 2.5-fold (90 ± 39 for control rats and 223 ± 45 for electrode-holding rats; *Student's t-test*, $p < 0.001$), thus indicating a noticeable activation of cell proliferation or migration at the spinal tissue under the array. To identify the contributing cell populations, we assess markers of neuronal, inflammatory, and vascular components.

Among neuronal markers, βIII-tubulin shows a modest but significant reduction (*Student's t-test*, $p = 0.007$), whereas MAP-2, a marker of mature neurons, did not show significant changes (*Student's t-test*, $p = 0.118$ in number and $p = 0.110$ in area). GAP43, a marker of axon growth cones, remarkably increased with respect to control rats (*Student's t-test*, $p = 0.002$), suggesting the occurrence of some plasticity phenomena driven by the presence of the electrode. The area occupied by GFAP$^+$ astrocytes slightly but significantly increased in rats holding the electrodes (*Student's t-test*, $p = 0.035$), again pointing to some moderate adaptation of the neural tissue below the electrode array.

Inflammation in the spinal tissue below the implanted electrode is almost negligible, although the number of macrophages (ED1$^+$) in the site slightly increased from 2 ± 3 cells per field in control rats to 21 ± 15 in electrode-holding rats (*Student's t-test*, $p < 0.001$), as well as its corresponding area (*Student's t-test*, $p = 0.008$). Importantly, the abundance of vimentin, a characteristic marker of scarring cells in the injured spinal cord, is not affected by the presence of the array (*Student's t-test*, $p = 0.061$), thus excluding the occurrence of any major damage to the spinal tissue in comparison to typical responses found at the injured spinal cord previously reported [53, 54]. Finally, we also explored the eventual alteration of the spinal vasculature (Figure 7e). Endothelial cells were not impacted by the presence of the electrode array, as reflected by the preservation of Reca-1$^+$ area (*Student's t-test*, $p = 0.114$). Moreover, the number of Reca-1$^+$ components moderately increased (207 ± 36 in control rats and 232 ± 49 in electrode-holding rats; *Student's t-test*, $p = 0.025$), what could guarantee nourishment of the slightly higher cell population filling the area. In line with this finding, laminin, a major component of the basal lamina of blood vessels, also increased in those rats holding the electrode array (*Student's t-test*, $p < 0.001$), in agreement with a larger number of vascular structures indicated by Reca-1 staining. Together, these results demonstrate that the MEsA undergoes complete biodegradation within four months while eliciting only moderate and localized tissue responses, without inducing major inflammation, neuronal loss, or fibrotic scarring.

3 | Conclusion

A fully maskless fabrication strategy for biodegradable PLA-based neural interfaces is presented, enabling the development of anatomically tailored multielectrode arrays, here demonstrated for cortical (MEcAs) and spinal (MEsAs) applications. The combination of laser patterned PLA substrates and PEDOT/PSS electrodeposition yields thin, flexible devices with stable electrochemical response in terms of EIS and voltage transient, and supporting safe delivery of higher stimulation currents. Both MEcAs and MEsAs exhibit stable electrochemical response over several weeks in vitro without abrupt changes over the entire ageing test period, thus suggesting the structural integrity and functional stability of the active portion of the devices is preserved.

In in vivo acute condition, MEcAs reliably record somatosensory evoked potentials with high signal quality and spatial specificity, as shown by SNR and Z-score analyses. These complementary measures capture both the strength of the evoked responses and their deviation from baseline activity, providing a solid framework for comparing contralateral and ipsilateral conditions.

MEsAs enable selective recruitment of sensory and motor spinal pathways, with stimulation thresholds and input–output relationships consistent with spinal anatomy and electrode geometry. Long-distance configurations, characterized by greater inter contact distance, consistently recruit more motor neurons, generate larger MEPs, and require lower thresholds than short configurations, likely due to multi-segment activation. Short-distance configurations provide higher spatial precision, enabling more localized modulation. Sensory responses (SEPs) exhibit similar geometry-dependent effects: long-distance configurations produce stronger SEPs but also greater inter-animal variability, reflecting anatomical differences and the sensitivity of dorsal column activation to electrode placement. Broader recruitment in

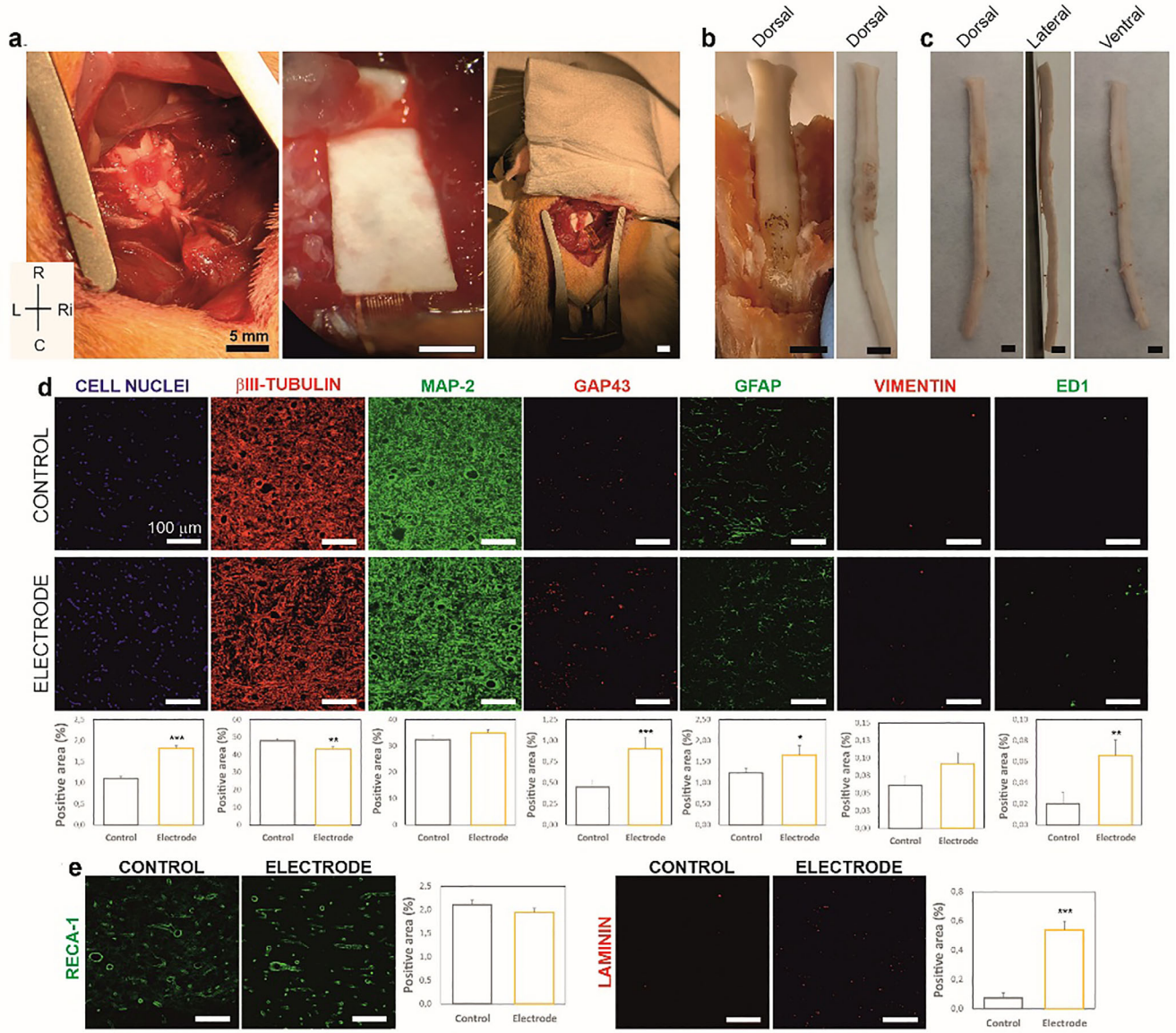

FIGURE 7 | (a) Intra-operatory photographs of the site of implantation illustrating the removal of C5 and C7 vertebra laminae (left), placement of Neuro-patch on top of the electrode (middle) and final disposition of the electrode, the protective patch and the vertebra laminae before closure. (b) Cervical column and extracted spinal cord right after perfusion of the rat showing the evident visualization of the gold components of the electrodes in close contact with the meninges. (c) Representative images of the spinal cord without meninges of one electrode-holding rat after perfusion and extraction. Scale bars in (a), (b) and (c) represent 5 mm. Immunofluorescence studies of (d) neural and inflammatory markers and (e) vascular markers at the cervical spinal tissue underneath the electrode. Representative confocal images are included for both control and electrode-holding rats. Scale bars in (d) and (e) represent 100 μm. Statistical analyses are performed by Student's t-test. Significance: $p < 0.05$*, $p < 0.01$** and $p < 0.005$***. C: Caudal, L: Left, R: Rostral, Ri: Right.

long-distance configurations may engage inhibitory subcortical mechanisms; whereas short-distance configurations may avoid lateral inhibition and favor localized facilitation. These results demonstrate that biodegradable arrays can support both high fidelity recording and effective stimulation.

Chronic implantation studies demonstrate that the PLA components of the arrays are almost completely resorbed and highly biocompatible up to four months after epidural placement. The PLA substrate fully degrades, leaving only the gold contacts, with no macroscopic alterations of the spinal cord and only mild, localized cellular responses consistent with physiological adaptation rather than tissue damage [53, 54]. A minor contribution of acidic PLA degradation byproducts cannot be excluded, and it will be investigated in future studies. Importantly, the vasculature remains preserved, and no glial scarring is observed.

A limitation identified in both MEcAs and MEsAs is the fragility of the contact pads, which represent the weakest element of the current design and can hamper connectivity and hence communication in the long term. Nevertheless, the stability of the active portion of the devices, together with the ageing test, the in vivo performance and biocompatibility assessment at chronic time points, indicates that these interfaces are suitable

and can be used and implemented for chronic monitoring studies. Future work will focus on longitudinal functional recording over the full degradation period by reinforcing and implementing a fixed connector to ensure stable and constant interfacing with external instrumentation throughout the chronic experiments. To the best of our knowledge, this is the first demonstration of a biodegradable epidural interface for spinal cord stimulation.

Together, these findings establish PLA-based MEcAs and MEsAs as a promising platform for transient neural interfaces, combining functional performance, biocompatibility, and biodegradation control. Future work will focus on reinforcing the electrical contact interface and validating long-term recording and stimulation paradigms in animal models.

4 | Experimental Section

4.1 | Device Fabrication

A PLA solution (Evonik Resomer R 207 S, 1% w/v in chloroform) is prepared and stirred for 2 h to ensure complete dissolution. Two sacrificial layers are fabricated by spin-coating 4 mL of polyacrylic acid (PAA, Mw 100 000, 35% in H_2O) onto glass Petri dishes (Laurell WS-650S-SNPP/Lite; 5 s at 800 rpm, then 40 s at 2000 rpm) and curing them in an oven (2 h, 60 °C). A volume of 8 mL of PLA solution is then cast onto each PAA layer and left at room temperature for 12 h to allow solvent evaporation, followed by thermal curing (2 h, 60 °C). After cooling, one PAA/PLA stack is immersed in distilled water for 24 h to dissolve the PAA and obtain a free-standing PLA film used as the insulating layer. This film is placed on a sensitized metallic surface and patterned by laser ablation (Nd:YAG, 16 W, 4 ns pulses, 100 kHz, 35 mm s^{-1}) to create openings for electrodes and connector pads. The second PAA/PLA stack is metallized with 5 nm Ti / 70 nm Au via thermal sublimation, monitored with a quartz microbalance. The electrode layout is transferred by laser ablation (16 W, 4 ns, 40 kHz, 100 mm s^{-1}), and the patterned film is released by water lift-off. The metallized PLA layer is mounted on a glass substrate, and alignment with the insulating PLA film is performed under optical microscopy (Leica Z16APO). The two layers are thermally sealed in a two-step process: 20 s on a 70 °C hot plate, followed by oven curing at 60 °C for 20 min. A polyimide spacer (4.8 mm × 4.8 mm × 0.2 mm) is attached to the backside of the connector region to ensure stable electrical contact with the Hirose FH26W-15S-0.3SHW connector.

4.2 | Atomic Force Microscopy Images

The surface topography of the electrodeposited PEDOT/PSS on ablated gold-polyimide substrates was investigated by atomic force microscopy (AFM), using Park XE7 AFM System (Park System, Suwon, Korea) operating in non-contact mode, in environmental conditions. Premounted silicon cantilevers (OMCL-AC160TS, Olympus Micro Cantilevers, Tokyo, Japan) with an Al backside reflective coating, a tip curvature radius of ca. 7 nm, an elastic constant of ca. 26 Nm^{-1}, and a resonance frequency of ca. 300 Hz were used. Image analysis and quantitative data extraction was performed with Park System XEI software (Park System, Suwon, Korea).

4.3 | Electrodeposition Protocol

PEDOT/PSS electrodeposition is performed in a two-electrode configuration using a Gamry Reference 600 potentiostat. A platinum mesh serves as the counter/reference electrode, while the microelectrodes act as the working electrode. Deposition is carried out under charge-controlled conditions until reaching a final charge density of 300 mC cm^{-2}. Potentiostatic electrodeposition of PEDOT/PSS (5s 0.2 V, then 0.8 V in charge limit control, up to the desired charge density), is carried out starting from an aqueous solution containing 10 mM EDOT and 5 mg mL^{-1} NaPSS.

4.4 | Electrochemical Impedance Spectroscopy Measurements

Impedance measurements of both bare and PEDOT/PSS-coated electrodes are performed using a Gamry Reference 600 potentiostat in physiological solution (sodium chloride 0.9%, Eurospital) in a two-electrode configuration. A platinum mesh short-circuited with the reference electrode serves as the counter electrode, while the electrodes on the arrays act as working electrodes. A sinusoidal wave with an amplitude of 10 mV and frequency spanning from 100 kHz to 1 Hz is applied to obtain impedance spectra.

4.5 | Chronopotentiometry

A Gamry Reference 600 potentiostat is used to carry out chronopotentiometry measurements in a phosphate buffer saline (PBS, Sigma Aldrich, 1 M) in a two-electrode configuration. The stimulation paradigm includes a 0 A baseline for 100 ms prior to the delivery of a biphasic current pulse. Each pulse has a duration of 200 µs and amplitudes ranging from 10 to 50 µA, resulting in a total biphasic pulse duration of 400 µs [55]. Due to instrument limitations, a non-zero inter-stimulus current between the cathodic and anodic phases is neither present nor monitored.

4.6 | Ageing test

An orbital shaker with a thermostatic hood (ASAL-711 CT) was used to maintain the samples at a constant temperature of 40 °C throughout the entire duration of the test. For the time-lapse imaging, four flasks (Corning, 25 mL) were filled with phosphate-buffered saline (PBS, Sigma Aldrich, 1 M), and one array was placed inside each flask. The flasks were then sealed with glue.

For electrochemical impedance spectroscopy (EIS) monitoring, six flasks (Corning, 25 mL) were drilled with two holes: one to host the array and a second to accommodate the Pt wire used as the counter electrode during EIS measurements (Figure S6). The array was inserted into the hole, and the contact-pad area was fixed externally on the surface of the flask using Kapton tape. In this configuration, the active area of the array was immersed in PBS, while the contact pads remained accessible for connection via a micromanipulator. The hole hosting the Pt wire was sealed

with Kapton tape, and the flask was filled with PBS. Each flask was then closed and the cap sealed with glue.

The ten samples were placed inside the thermostatic hood together with an additional PBS-filled flask equipped with a wireless temperature sensor. This sensor allowed continuous monitoring of the bath temperature by recording a temperature value every 30 s for the entire experiment.

Measurements were performed every 7 days. Time-lapse images were acquired using a Nikon Coolpix B500, and EIS measurements were carried out with a Gamry Potentiostat 600, as described in the Impact of aging on arrays and electrochemical impedance spectroscopy section.

4.7 | Bilateral barrel cortex surgery and electrophysiological recordings

Experiments were performed in compliance with the guidelines established by the European Communities Council (Directive 86/609/EEC, 24 November 1986) and the Italian Legislative Decree n. 26 (4/3/2014). The protocol was approved by the Ethics Committee for animal research of the University of Ferrara and by the Italian Ministry of Health (permission n. 989/2020-PR).

MEcAs were assessed in vivo in two adult Long Evans rats (males, 300–400 g) implanted over the primary somatosensory cortex (barrel field, S1BF). The surgical procedures for exposing the barrel cortex, implanting the device, and eliciting somatosensory evoked potentials (SEPs) followed previously described protocols [56, 57]. Briefly, animals were anesthetized with Zoletil (Virbac, France; 30 mg kg^{-1}, i.p.). Anesthesia depth was monitored throughout the procedure by verifying the absence of the hind-limb withdrawal reflex and maintained with additional intramuscular doses as needed. The animals were then placed in a stereotaxic frame (David Kopf Instruments, USA) equipped with ear bars (Model 957 for small animals). A ≈3-cm midline incision was made, and the overlying muscle and connective tissue were removed to expose the skull.

Two bilateral craniotomies (≈6 × 6 mm^2 each) were performed over the parietal bone to expose the barrel cortex on both hemispheres, enabling ipsilateral and contralateral recordings relative to the stimulated right whisker. A stainless-steel bone screw was inserted in the contralateral parietal bone to serve as ground. Each device was placed epidurally over the corresponding barrel cortex.

As a further control on the reliability of signal recorded with MEcA, the craniotomies were subsequently enlarged to expose the Parietal Cortex bilaterally, while preserving the midline bone ridge separating the two hemispheres. Signal was acquired in the Parietal Cortex bilaterally on both hemispheres during whiskers stimulation.

Whisker stimulation was delivered using a vibrating system producing a horizontal multi-whisker deflection. The whiskers contralateral to the craniotomy were trimmed and inserted into a Velcro strip attached to a rod driven by a shaker (Type 4810 mini shaker, Bruel & Kjaer, Denmark) controlled by a National Instruments board (Austin, USA). The stimulus consisted of a 12-ms sine waveform producing a 500-μm whisker deflection, repeated 60 times. Neural signals were acquired at 20 kHz using an Intan RHD amplifier/digitizer module. For each rat, different positions and orientations of the ECoG devices over the barrel cortex were investigated in order to evaluate the device reliability in detecting a well-known neurophysiological signal such as the somatosensory evoked potentials (SEPs). To minimize electromagnetic interference, recordings were performed inside a Faraday cage.

At the end of the experiment, animals were euthanized with an intracardiac injection of Tanax (0.3 mL kg^{-1}).

4.8 | Spinal Surgery, Acute Stimulation and Neural Recordings

All procedures were approved by the Ethical Committee for Animal Research of the *Hospital Nacional de Parapléjicos* (Toledo, Spain; 55 OH/2022) and carried out in accordance with the ARRIVE guidelines, the International Council for Laboratory Animal Science, and the European Union 2010/63/EU Guideline. Adult male and female Wistar rats (5 months old) were used. Animals were group housed in a temperature-controlled environment under a 12 h light/dark cycle, with food and water available ad libitum. All efforts were made to minimize animal use and suffering, following the 3Rs principles.

Rats were anesthetized with isoflurane (3% in 2 L O_2/min for induction; 1.5–2% in 2 L O_2/min for maintenance) and placed in a stereotaxic frame. Body temperature was maintained at 36.5 °C using a homoeothermic blanket (Cibertec SL, Madrid, Spain), and the eyes were protected with vaseline (Kern Pharma). A cranial surgical procedure was first performed to implant electrodes for electroencephalography (EEG) and somatosensory evoked potential (SEP) recordings. Lidocaine (2%) was injected subcutaneously into the scalp, after which a rostrocaudal incision was made and the skin and muscles retracted. The periosteum was removed, and two stainless steel screws (1 × 4 mm) were bilaterally implanted over the hindlimb region of the primary somatosensory cortex (HLCx) (from bregma: AP −1.5 to −1.7 mm; ML 2.3 mm). A third screw was placed 1 mm caudal to lambda and used as a common reference. Correct placement of the electrodes was verified by recording SEPs evoked by electrical stimulation of the hindlimb ankle using two subcutaneous needle electrodes in a bipolar configuration (Zaforas et al., 2024, STAR Protocols).

A second surgical procedure was then performed to expose the lumbar spinal cord (L1–L3) for implantation of the MEsA used for epidural stimulation. After shaving and disinfecting the dorsal area, a midline incision was made from T12 to L3, and the paraspinal muscles were carefully separated to expose the vertebrae. Once the spinal cord was exposed, the electrode array was positioned epidurally with the midline aligned between the two rows of electrodes (Figure 6a). For EMG recordings, a 10 mm active needle electrode was inserted into the right biceps femoris (posterior), and a reference electrode was placed at the ankle.

To characterize the stimulation properties of the array, four epidural stimulation configurations were tested: (a) short linear (electrodes 2–6), (b) long linear (electrodes 2–10), (c) short

crossed (electrodes 2–3), and (d) long crossed (electrodes 2–11). Stimulation was delivered at 1 Hz with 50–100 μs pulses, and intensity was gradually increased from 0.1 to 0.8 mA. After reaching threshold, intensity increments followed this sequence: 0.025 mA for four stimuli, 0.05 mA for two stimuli, 0.1 mA for two stimuli, and 0.2 mA for the final steps to construct the recruitment curve. Stimulation was delivered using a CS 420 digital stimulator (Cibertec S.A.) and an ISO Flex isolator (A.M.P.I.). Parameters were selected to evoke measurable responses without producing overt hindlimb movements.

Electrophysiological signals (EEG and EMG) were recorded using a modular system (Neurolog; Digitimer) including preamplifier, filters, and amplifier. Signals were acquired in DC mode, filtered up to 3 kHz, amplified ×500, and digitized at 20 kHz using a CED Power1401 interface (Cambridge Electronic Design, UK). Online visualization was performed with Spike2 software to ensure correct stimulation and recording.

4.9 | Chronic Epidural Array Implantation Surgery

All animal procedures were performed in accordance with the European Union guidelines (Directive 2010/63/EU) and approved by the Ethical Committee for Animal Research at the *Hospital Nacional de Parapléjicos* and the Dirección General de Agricultura y Ganadería of Castilla-La Mancha (reference number 3–2023). Six adult male Wistar rats (approximately 3 months old) were used in this study, three serving as controls and three undergoing a triple laminectomy followed by epidural implantation of the MEsAs. MEsAs underwent UV sterilization (germicidal UV-C band, 254 nm, 30 min per side in a biosafety cabinet) prior to chronic implantation. Animals were housed in standardized cages (two per cage) under a 12 h light/dark cycle at 23 °C, with food and water available ad libitum in a non-enriched environment.

For the surgical procedure, rats were anesthetized with sodium pentobarbital (55 mg kg^{-1}) mixed with atropine (0.05 mg kg^{-1}), and xylazine (10 mg kg^{-1}) was administered intraperitoneally as an analgesic and muscle relaxant. Ophthalmic gel (Lubrithal, Dechra) was applied to protect the eyes, and body temperature was maintained at 36.5 °C using an automatically controlled heating pad (Cibertec SL, Madrid, Spain). After shaving and disinfecting the surgical area with betadine, a midline incision was made from the base of the skull to the T3 vertebral level. Muscle layers were carefully dissected and retracted while preserving most musculature and major blood vessels. The laminae of the C5–C7 vertebrae were then sequentially removed, and the electrode array was gently positioned epidurally in close contact with the meninges of the exposed spinal segments. A microporous patch (Neuro-patch, Braun) was placed over the device to protect the spinal cord from scar tissue originating from the overlying muscle layers and to prevent array displacement. The removed vertebral laminae were repositioned on top of the patch to provide additional mechanical reinforcement. Deep and superficial muscles were sutured with a bioresorbable suture and the skin closed with a similar suture. During the first three postoperative days, animals received meloxicam (5 mg mL^{-1}, 0.1 mL kg^{-1} every 12 h, subcutaneous; Boehringer Ingelheim), enrofloxacin (2.5%, 25 mg mL^{-1}, 0.3 mL kg^{-1} every 24 h, subcutaneous; Bayer), and 5 mL of saline solution (B. Braun Medical, S.A.). After four months of implantation, animals were euthanized following a standard perfusion-fixation protocol. Spinal cords were extracted and examined macroscopically to exclude signs of gross damage prior to histological processing.

4.10 | Histological Studies

Antibodies and chemical reagents for histological studies were purchased from Merck and used as received unless otherwise indicated. Perfused spinal cord samples were kept overnight in 4% paraformaldehyde at 4 °C and then transferred to 30% sucrose in phosphate buffered saline (PBS) for 3 days at 4 °C for cryoprotection. Tissue pieces were mounted on plastic supports and rapidly frozen in Optimal Cutting Temperature compound (Tissue Tek, Hatfield, PA). The entire spinal fragment was sectioned sagittally from right to left into 10 μm slices using a Leica CM1900 cryostat set at a 10° angle.

4.11 | Immunofluorescence Studies

Antibodies and chemical reagents for immunofluorescence were purchased from Merck and used as received unless otherwise indicated. Spinal cord sections were processed to detect the following markers: (1) microtubule associated protein 2 (MAP 2; M1406, 1:500, Merck) and (2) βIII tubulin (T2200, 1:500, Merck) for somas and neurites in neurons; (3) vimentin (SAB4300676, 1:500, Merck) for non-neuronal cells including glial and connective tissue cells; (4) glial fibrillary acidic protein (GFAP; G3893, 1:400, Merck) for astrocytes; (5) ED1 (MAB1435, 1:100, Chemicon) for macrophages; (6) RECA 1 (MCA970R, 1:250, Bio Rad) for endothelial cells; (7) laminin (LS C96142, 1:500, LSBio) for vascular basal laminae; and (8) GAP 43 for neuronal growth cones. Appropriate secondary antibodies were used for each primary antibody. Cell nuclei were counterstained with Hoechst (1 mg mL^{-1}). Fluorescence images were acquired using a Leica resonant SP5 microscope. Imaging parameters were fixed using control sections incubated with secondary antibodies only, and all images were subsequently acquired under identical conditions.

Fluorescence quantification was performed automatically using a custom Fiji macro, measuring the number of positively stained pixels (μm^2) for each marker after defining the appropriate threshold. The number of positive counts per image was also evaluated when relevant. Control spinal cords were used to establish threshold values for each marker. At least five non-overlapping images per animal were analyzed ($N \geq 15$ per marker and group).

4.12 | Data Analysis for Bilateral Microelectrocorticography

All analyses were performed in MATLAB (R2023b, MathWorks). Epicortical signals were sampled at 20 kHz and preprocessed using a two-stage filtering pipeline. A fourth order IIR notch filter (49–51 Hz) was first applied to suppress line noise, followed by a fourth order Butterworth band-pass filter (3–400 Hz). Both

filters were implemented in zero-phase mode using the MATLAB function filtfilt to avoid phase distortions.

4.13 | Evoked Activity (SEPs)

For somatosensory evoked potential (SEP) analysis, contralateral and ipsilateral recordings were segmented into 100-ms windows aligned to the TTL trigger. For each electrode (n = 9) and each trial, the corresponding segment was extracted, and trial-averaged waveforms were computed to obtain the mean SEP response. Ipsilateral traces, which did not exhibit stimulus-locked activity, served as internal controls.

4.14 | Spectral Analysis of Evoked Responses

Spectral analyses were performed on two 80-ms windows: a post-stimulus window corresponding to the evoked response, and a baseline window positioned 1 s before stimulation. For each trial and channel, power spectral density (PSD) was estimated using Welch's method with a 50-ms Hamming window, 50% overlap, and a 4096-point FFT. Band-limited power was computed by integrating the PSD between 5 and 300 Hz. This band-power metric was used consistently across all subsequent analyses.

4.15 | Signal to Noise Ratio (SNR)

To quantify the magnitude of the evoked response relative to spontaneous activity, the signal-to-noise ratio (SNR) was computed for each trial and channel as SNR = Pstim/Pbase, where

Pstim and Pbase denote the post-stimulus (evoked activity) and baseline (pre-stimulus spontaneous activity) band-power, respectively. The same procedure was applied to ipsilateral recordings. Mean SNR values and their standard errors were then calculated across trials for each electrode.

4.16 | Z-Score Analysis

To assess statistical significance, Z-scores were computed for each trial and channel as: Z = (Pstim−μbase)/σbase, where Pstim denotes the post stimulus band power (5–300 Hz), and μbase and σbase represent the mean and standard deviation of the baseline band power, respectively. Z-scores were computed using the same band power values used for SNR. The same procedure was applied to ipsilateral recordings. For each electrode, mean values of stimulus power, baseline power, ipsilateral power, SNR, and Z-scores were used to generate spatial power maps and contralateral–ipsilateral comparisons.

4.17 | Spontaneous Activity Analysis

To characterize spontaneous cortical activity, 10-s segments of spontaneous recordings were analyzed for both hemispheres. PSDs were computed for raw, notch-filtered, and band-pass–filtered signals. For each channel, PSD estimation was performed using Welch's method with a 2-s Hamming window, 50% overlap, and an FFT length set to the next power of two above the window size to optimize computational efficiency. PSDs from individual channels were then averaged to obtain hemisphere-level spectral profiles. For quantitative comparison, PSD values were restricted to the 5–300 Hz frequency range. Contralateral and ipsilateral spectra were compared across the three preprocessing conditions (raw, notch-filtered, and band-pass–filtered), enabling assessment of spontaneous spectral content, filtering effects, and potential hemispheric differences unrelated to sensory stimulation.

4.18 | Data Analysis for Spinal Stimulation

All electrophysiological data were stored for offline processing using Spike2 (v7, Cambridge Electronic Design, UK). Signals were digitally filtered, and evoked responses were analyzed within predefined post-stimulus windows: 5–30 ms for SEPs and 1–8 ms for MEPs. For each condition, the peak-to-peak amplitude (mV) of individual SEPs occurring during cortical down-states and of MEPs was measured. Amplitudes were then averaged across trials to obtain the final evoked response values.

4.19 | Statistics

Data from biodegradability and biocompatibility assessment are expressed as mean ± standard error of the mean (SEM) from three animals per group (N = 3). Statistical analysis was performed using the Statistical Package for the Social Sciences (SPSS version 30.0). Comparisons 0 the two experimental groups were conducted using a Student's t-test. Significance levels were defined as $p \leq 0.05$*, $p \leq 0.01$**, and $p \leq 0.005$***.

Acknowledgements

The Service of Microscopy and Image Analysis at the Hospital Nacional de Parapléjicos is acknowledged for assistance with confocal studies.

Open access publishing facilitated by Istituto Italiano di Tecnologia, as part of the Wiley - CRUI-CARE agreement.

Funding

This work has received funding from the: European Union's Horizon Europe research and Innovation Programme under grant agreement No. 101098597 (Piezo4Spine) ICMM-CSIC acknowledges the Severo Ochoa Centres of Excellence program through Grant CEX2024-001445-S/ funded by MICIU/AEI / 10.13039/501100011033. Spanish Ministry of Science and Innovation MCIN/AEI/10.13039/501100011033 to J.M.R. (grant RYC2019-026870-I, co-funded by "'ESF Investing in your future"'). Italian Ministry of Health under grant agreement PNRR-POC-2022-12376380, project BLBC. This work was conducted within the Technologies for Healthy Living Flagship and Brain and Machines Flagship of the Istituto Italiano di Tecnologia.

Conflicts of Interest

None of the authors have a conflict of interest to disclose.

Data Availability Statement

All data needed to evaluate the conclusions in the paper are present in the paper or the Supporting Information. Data available from the authors upon reasonable request

References

1. X. Lin, X. Zhang, J. Chen, and J. Liu, "Material Selection and Device Design of Scalable Flexible Brain-Computer Interfaces: A Balance Between Electrical and Mechanical Performance," *Advanced Materials* 37 (2025): 2413938, https://doi.org/10.1002/adma.202413938.

2. M. Habibollahi, D. Jiang, H. T. Lancashire, and A. Demosthenous, "Active Neural Interface Circuits and Systems for Selective Control of Peripheral Nerves: A Review," *IEEE Transactions on Biomedical Circuits and Systems* 18 (2024): 954–975, https://doi.org/10.1109/TBCAS.2024.3430038.

3. G. Buzsáki, C. A. Anastassiou, and C. Koch, "The origin of extracellular fields and currents — EEG, ECoG, LFP and spikes," *Nature Reviews Neuroscience* 13 (2012): 407–420, https://doi.org/10.1038/nrn3241.

4. D. Yang, G. Tian, J. Chen, et al., "Neural electrodes for brain-computer interface system: From rigid to soft," *BMEMat* 3 (2025): 12130.

5. A. Carnicer-Lombarte, S.-T. Chen, G. G. Malliaras, and D. G. Barone, "Foreign Body Reaction to Implanted Biomaterials and Its Impact in Nerve Neuroprosthetics," *Frontiers in Bioengineering and Biotechnology* 9 (2021): 622524, https://doi.org/10.3389/fbioe.2021.622524.

6. "Implants that vanish," *Nature Biomedical Engineering* 3 (2019): 585, https://doi.org/10.1038/s41551-019-0449-5.

7. I. Dasgupta, E. Klein, L. Y. Cabrera, et al., "What Happens After a Neural Implant Study? Neuroethics Expert Workshop on Post-Trial Obligations," *Neuroethics* 17 (2024): 22, https://doi.org/10.1007/s12152-024-09549-2.

8. H. Mirzajani, P. Zolfaghari, S. Akbari Nakhjavani, B. Y. Koca, M. Khodapanahandeh, and H. Urey, "Transient Implantable Electronics for Postsurgery Preventive Medicine," *Advanced Functional Materials* 35 (2025): 2413324, https://doi.org/10.1002/adfm.202413324.

9. Y. Zhang, G. Lee, S. Li, Z. Hu, K. Zhao, and J. A. Rogers, "Advances in Bioresorbable Materials and Electronics," *Chemical Reviews* 123 (2023): 11722–11773, https://doi.org/10.1021/acs.chemrev.3c00408.

10. F. Alam, M. Ashfaq Ahmed, A. Jalal, et al., "Recent progress and challenges of implantable biodegradable biosensors," *Micromachines* 15 (2024): 475.

11. J.-K. Chang, H. Fang, C. A. Bower, E. Song, X. Yu, and J. A. Rogers, "Materials and processing approaches for foundry-compatible transient electronics," *Proceedings of the National Academy of Science USA* 114 (2017): E5522–E5529, https://doi.org/10.1073/pnas.1707849114.

12. K. Chen, W. Yu, G. Zheng, et al., "Biomaterial-based regenerative therapeutic strategies for spinal cord injury," *NPG Asia Materials* 16 (2024): 5, https://doi.org/10.1038/s41427-023-00526-4.

13. A. Weiss, Y. Ding, and M. Rodriguez, "A literature review on neuron scaffolding for repairing peripheral nerves: Advances, challenges, and future directions," *Brain Circulation* 11 (2025): 266–275, https://doi.org/10.4103/bc.bc_138_24.

14. K. J. Yu, D. Kuzum, S.-W. Hwang, et al., "Bioresorbable silicon electronics for transient spatiotemporal mapping of electrical activity from the cerebral cortex," *Nature Materials* 15 (2016): 782–791, https://doi.org/10.1038/nmat4624.

15. K. Xu, S. Li, S. Dong, et al., "Bioresorbable Electrode Array for Electrophysiological and Pressure Signal Recording in the Brain," *Advanced Healthcare Materials* 8 (2019): 1801649, https://doi.org/10.1002/adhm.201801649.

16. M. Cho, J.-K. Han, J. Suh, et al., "Fully bioresorbable hybrid opto-electronic neural implant system for simultaneous electrophysiological recording and optogenetic stimulation," *Nature Communications* 15 (2024): 2000, https://doi.org/10.1038/s41467-024-45803-0.

17. P. Zhang, Y. Yang, Z. Li, et al., "Conducting Hydrogel-Based Neural Biointerfacing Technologies," *Advanced Functional Materials* 35 (2025): 2422869, https://doi.org/10.1002/adfm.202422869.

18. M. Wu, K. Yao, N. Huang, et al., "Ultrathin, Soft, Bioresorbable Organic Electrochemical Transistors for Transient Spatiotemporal Mapping of Brain Activity," *Advanced Science* 10 (2023): 2300504, https://doi.org/10.1002/advs.202300504.

19. G. Schiavone, F. Fallegger, X. Kang, et al., "Soft, Implantable Bioelectronic Interfaces for Translational Research," *Advanced Materials* 32 (2020): 1906512, https://doi.org/10.1002/adma.201906512.

20. B. Harland, L. Matter, S. Lopez, et al., "Daily electric field treatment improves functional outcomes after thoracic contusion spinal cord injury in rats," *Nature Communications* 16 (2025): 5372, https://doi.org/10.1101/2024.11.01.621450.

21. B. Harland, Z. Aqrawe, M. Vomero, et al., "A Subdural Bioelectronic Implant to Record Electrical Activity from the Spinal Cord in Freely Moving Rats," *Advanced Science* 9 (2022): 2105913, https://doi.org/10.1002/advs.202105913.

22. C. Kathe, F. Michoud, P. Schönle, et al., "Wireless closed-loop optogenetics across the entire dorsoventral spinal cord in mice," *Nature Biotechnology* 40 (2022): 198–208, https://doi.org/10.1038/s41587-021-01019-x.

23. I. R. Minev, P. Musienko, A. Hirsch, et al., "Electronic dura mater for long-term multimodal neural interfaces," *Science* 347 (2015): 159–163, https://doi.org/10.1126/science.1260318.

24. T. Milekovic, E. M. Moraud, N. Macellari, et al., "A spinal cord neuroprosthesis for locomotor deficits due to Parkinson's disease," *Nature Medicine* 29 (2023): 2854–2865, https://doi.org/10.1038/s41591-023-02584-1.

25. V. C. Pinto, T. Ramos, S. Alves, et al., "Comparative Failure Analysis of PLA, PLA/GNP and PLA/CNT-COOH Biodegradable Nanocomposites thin Films," *Procedia Engineering* 114 (2015): 635–642, https://doi.org/10.1016/j.proeng.2015.08.004.

26. S. Farah, D. G. Anderson, and R. Langer, "Physical and mechanical properties of PLA, and their functions in widespread applications — A comprehensive review," *Advanced Drug Delivery Reviews* 107 (2016): 367–392, https://doi.org/10.1016/j.addr.2016.06.012.

27. W. Xu, N. Chahine, and T. Sulchek, "Extreme Hardening of PDMS Thin Films Due to High Compressive Strain and Confined Thickness," *Langmuir* 27 (2011): 8470–8477, https://doi.org/10.1021/la201122e.

28. B. Rubehn and T. Stieglitz, "In vitro evaluation of the long-term stability of polyimide as a material for neural implants," *Biomaterials* 31 (2010): 3449–3458, https://doi.org/10.1016/j.biomaterials.2010.01.053.

29. M. Vomero, M. F. Porto Cruz, E. Zucchini, et al., "Conformable polyimide-based μECoGs: Bringing the electrodes closer to the signal source," *Biomaterials* 255 (2020): 120178, https://doi.org/10.1016/j.biomaterials.2020.120178.

30. M. Hussain, S. M. Khan, M. Shafiq, and N. Abbas, "A review on PLA-based biodegradable materials for biomedical applications," *Giant* 18 (2024): 100261.

31. R. Stendel, B. Krischek, and T. A. Pietila, "Biodegradable Implants in Neurosurgery," *Acta Neurochirurgica* 143 (2001): 237–243, https://doi.org/10.1007/s007010170103.

32. P. I. J. M. Wuisman and T. H. Smit, "Bioresorbable polymers: Heading for a new generation of spinal cages," *European Spine Journal* 15 (2006): 133–148, https://doi.org/10.1007/s00586-005-1003-6.

33. M. Bianchi, A. De Salvo, M. Asplund, et al., "Poly(3,4-ethylenedioxythiophene)-Based Neural Interfaces for Recording and Stimulation: Fundamental Aspects and In Vivo Applications," *Advanced Science* 9 (2022): 2104701, https://doi.org/10.1002/advs.202104701.

34. P. Sun, C. Li, C. Yang, et al., "A biodegradable and flexible neural interface for transdermal optoelectronic modulation and regeneration of peripheral nerves," *Nature Communications* 15 (2024): 4721, https://doi.org/10.1038/s41467-024-49166-4.

35. K. Alò, C. Varga, E. Krames, et al., "Factors affecting impedance of percutaneous leads in spinal cord stimulation," *Neuromodulation: Technology at the Neural Interface* 9 (2006): 128–135.

36. J. J. Lee, R. K. Simpson, and B. Dalm, "Permanent Paddle-lead Trial for Spinal Cord Stimulation," *Cureus* 10 (2018): 2645, https://doi.org/10.7759/cureus.2645.

37. H. Lorach, A. Galvez, V. Spagnolo, et al., "Walking naturally after spinal cord injury using a brain–spine interface," *Nature* 618 (2023): 126–133, https://doi.org/10.1038/s41586-023-06094-5.

38. P. Konrad, K. R. Gelman, J. Lawrence, et al., "First-in-human experience performing high-resolution cortical mapping using a novel microelectrode array containing 1024 electrodes," *Journal of Neural Engineering* 22 (2025): 026009, https://doi.org/10.1088/1741-2552/adaeed.

39. Y. Xie, Y. Peng, J. Guo, et al., "Materials and devices for high-density, high-throughput micro-electrocorticography arrays," *Fundamental Research* 5 (2025): 17–28, https://doi.org/10.1016/j.fmre.2024.01.016.

40. C. Welker and T. A. Woolsey, "Structure of layer IV in the somatosensory neocortex of the rat: Description and comparison with the mouse," *Journal of Comparative Neurology* 158 (1974): 437–453, https://doi.org/10.1002/cne.901580405.

41. E. L. Portiansky, F. Nishida, C. G. Barbeito, E. J. Gimeno, and R. G. Goya, "Increased number of neurons in the cervical spinal cord of aged female rats," *PLoS One* 6 (2011): 22537.

42. A. Toossi, B. Bergin, M. Marefatallah, et al., "Comparative neuroanatomy of the lumbosacral spinal cord of the rat, cat, pig, monkey, and human," *Scientific Reports* 11 (2021): 1955, https://doi.org/10.1038/s41598-021-81371-9.

43. X. T. Cui and D. D. Zhou, "Poly (3,4-Ethylenedioxythiophene) for Chronic Neural Stimulation," *IEEE Transactions on Neural System and Rehabilitation Engineering* 15 (2007): 502–508, https://doi.org/10.1109/TNSRE.2007.909811.

44. H. Zhou, X. Cheng, L. Rao, T. Li, and Y. Y. Duan, "Poly(3,4-ethylenedioxythiophene)/multiwall carbon nanotube composite coatings for improving the stability of microelectrodes in neural prostheses applications," *Acta Biomaterialia* 9 (2013): 6439–6449, https://doi.org/10.1016/j.actbio.2013.01.042.

45. M. Ganji, A. Tanaka, V. Gilja, E. Halgren, and S. A. Dayeh, "Scaling Effects on the Electrochemical Stimulation Performance of Au, Pt, and PEDOT:PSS Electrocorticography Arrays," *Advanced Functional Materials* 27 (2017): 1703019, https://doi.org/10.1002/adfm.201703019.

46. R. Vatsyayan and S. A. Dayeh, "A universal model of electrochemical safety limits in vivo for electrophysiological stimulation," *Frontiers in Neuroscience* 16 (2022): 972252, https://doi.org/10.3389/fnins.2022.972252.

47. W. Lei, C. Peng, S. Chiu, et al., "All Biodisintegratable Hydrogel Biohybrid Neural Interfaces with Synergistic Performances of Microelectrode Array Technologies, Tissue Scaffolding, and Cell Therapy," *Advanced Functional Materials* 34 (2024): 2307365, https://doi.org/10.1002/adfm.202307365.

48. C. C. H. Petersen, "The Functional Organization of the Barrel Cortex," *Neuron* 56 (2007): 339–355, https://doi.org/10.1016/j.neuron.2007.09.017.

49. C. C. H. Petersen, "Sensorimotor processing in the rodent barrel cortex," *Nature Reviews Neuroscience* 20 (2019): 533–546, https://doi.org/10.1038/s41583-019-0200-y.

50. A. Canedo and J. Aguilar, "Spatial and cortical influences exerted on cuneothalamic and thalamocortical neurons of the cat," *European Journal of Neuroscience* 12 (2000): 2515–2533, https://doi.org/10.1046/j.1460-9568.2000.00107.x.

51. A. Hirata, J. Aguilar, and M. A. Castro-Alamancos, "Influence of Subcortical Inhibition on Barrel Cortex Receptive Fields," *Journal of Neurophysiology* 102 (2009): 437–450, https://doi.org/10.1152/jn.00277.2009.

52. C. Soto, J. Aguilar, F. Martín-Cora, C. Rivadulla, and A. Canedo, "Intracuneate mechanisms underlying primary afferent cutaneous processing in anaesthetized cats," *European Journal of Neuroscience* 19 (2004): 3006–3016, https://doi.org/10.1111/j.0953-816X.2004.03432.x.

53. A. Domínguez-Bajo, A. González-Mayorga, C. R. Guerrero, et al., "Myelinated axons and functional blood vessels populate mechanically compliant rGO foams in chronic cervical hemisected rats," *Biomaterials* 192 (2019): 461–474, https://doi.org/10.1016/j.biomaterials.2018.11.024.

54. M. Zaforas, E. Benayas, R. Madroñero-Mariscal, et al., "Graphene oxide scaffolds promote functional improvements mediated by scaffold-invading axons in thoracic transected rats," *Bioactive Materials* 47 (2025): 32–50, https://doi.org/10.1016/j.bioactmat.2024.12.031.

55. M. Vomero, E. Zucchini, E. Delfino, et al., "Glassy Carbon Electrocorticography Electrodes on Ultra-Thin and Finger-Like Polyimide Substrate: Performance Evaluation Based on Different Electrode Diameters," *Materials* 11 (2018): 2486, https://doi.org/10.3390/ma11122486.

56. M. Vomero et al., "Achieving Ultra-Conformability With Polyimide-Based ECoG Arrays," *2018 40th Annual International Conference of the IEEE Engineering in Medicine and Biology Society (EMBC)* (2018): pp. 4464–4467, https://doi.org/10.1109/EMBC.2018.8513171.

57. M. di Lauro, E. Zucchini, A. de Salvo, et al., "A Novel Biasing Scheme of Electrolyte-Gated Organic Transistors for Safe In Vivo Amplification of Electrophysiological Signals," *Advanced materials interfaces* 9 2022: 2101798, https://doi.org/10.1002/admi.202101798.

Supporting Information

Additional supporting information can be found online in the Supporting Information section.

Supporting File: admi70601-sup-0001-SuppMat.docx.